Supplementary Information of

Three-degree-of-freedom measurement using a single probe beam

Liheng Shi[1,2], Jinxu Zhang[1], Jiayang Chen[1], Runkun Zhao[1], Yuxuan Ma[1], Chen Lin[1], Siyu Zhou[1], Lijiang Zeng[1] and Guanhao Wu[1,*]

[1]*State Key Laboratory of Precision Measurement Technology and Instruments, Department of Precision Instrument, Tsinghua University, Beijing 100084, China*

[2]*Research Center of Opto-electronic Sensing, Yangtze Delta Region Institute of Tsinghua University, Zhejiang, Zhejiang 314006, China*

**Corresponding author: guanhaowu@mail.tsinghua.edu.cn*

This Supplementary Information consists of the following sections:

S1. Comparison with other methods

The table below presents the state-of-the-art optical multiple DOF measurement methods across various fields, detailing the type of each DOF measurable (absolute or relative measurement), measurement principles, target types, and the number of beams (including both illumination and reception). Among these, in precision instruments and manufacturing, where high accuracy is demanded, interferometric methods are primarily used, sometimes in conjunction with geometric optical methods. To achieve multiple DOF measurement, complex targets must be assembled, and multiple beams with spatial separation are employed. References [30] and [32] can measure non-cooperative targets but are limited to measuring relative pose changes through multiple beams. The advantage of the proposed LCSI is its ability to measure the absolute values of three DOFs of (multiple) non-cooperative targets using a single beam, a difficult to achieve by other methods. Notably, the measurable DOFs of this method complement those of ref. [48], and they can share system configurations and targets, allowing for an easy integration to simultaneously measure six DOFs.

Table S1. Comparison with other state-of-the-art optical multiple DOF measurement methods

Author	DOF	Principle	Target type	Beam	Application
Xu et al. [13]	x (absolute)	Vision	Visual scene with identifiable features	None	Visual navigation
	y (absolute)	Vision			
	z (absolute)	Vision			
	θ_x (absolute)	Vision			
	θ_y (absolute)	Vision			
	θ_z (absolute)	Vision			
RENISAW™ [49]	x (absolute)	Geometry	Triple corner-cube reflector and a rotation detector assembly	Seven parallel beams	Correction for the linear error in linear motion path
	y (absolute)	Geometry			
	z (relative)	Interferometry			
	θ_x (relative)	Interferometry			
	θ_y (relative)	Interferometry			
	θ_z (absolute)	Polarization			
Ma et al. [15]	x (absolute)	Geometry	Dual corner-cube retroreflector array	Four parallel beams	Correction for the linear error in linear motion path
	y (absolute)	Geometry			
	z (relative)	Interferometry			
	θ_x (absolute)	Geometry			
	θ_y (absolute)	Geometry			
	θ_z (absolute)	Geometry			

Author	DOF	Principle	Target type	Beam	Application
Zhou et al. [18,25]	x (absolute) y (absolute) z (absolute) θ_x (absolute) θ_y (absolute) θ_z (absolute)	Geometry Geometry Interferometry Interferometry Interferometry Geometry	Grating-corner-cube	Five parallel beams	Satellite formation flying and other space applications
Hsieh et al. [26]	x (relative) y (relative) z (relative) θ_x (relative) θ_y (relative) θ_z (relative)	Interferometry Interferometry Interferometry Interferometry Interferometry Interferometry	Two-dimensional transmission grating	Three focused beams	Precision stage positioning
Shi et al. [29]	θ_x (relative) θ_y (relative) θ_z (relative)	Interferometry Interferometry Interferometry	Rough plane	Four beams	Detection of minor structural deformations
Xu et al. [31]	z (relative) θ_x (relative)	Interferometry Interferometry	Non-cooperative cylinder	Two parallel beams	Lathe calibration and motor control
Hu et al. [32]	θ_x (absolute) θ_y (absolute)	Interferometry Interferometry	Plano mirror	Single beam	Lathe calibration and components alignment
Li et al. [48]	x (absolute) y (absolute) θ_z (absolute)	Vision Vision Vision	Target with identifiable features	None	Automatic control of in-plane motion
Proposed LCSI	z (absolute) θ_x (absolute) θ_y (absolute)	Coherence Coherence Coherence	Non-cooperative plane	Single beam	Component alignment, deformation detection, multi-target coordination, et al.

It's worth noting that precision is highly dependent on the specific measurement scenario and target type, so a direct comparison across different methods may not be fair. Instead, each approach is optimized for its intended application, and the focus here is on the unique strengths of LCSI, particularly in its ability to measure absolute DOFs of non-cooperative targets with a single beam.

Reference

[49] RENISAW. XM-60 multi-axis calibrator. https://www.renishaw.com/en/xm-60-and-xm-600-multi-axis-calibrator--39258 (2024).

S2. Measurement principle for low-coherence spatial interferometry (LCSI)

The system configuration of LCSI is illustrated in Fig. S1a. Low-coherence light is collimated and then incident onto a Twyman-Green interferometer, where the reference mirror R is perpendicular to the optical axis, and the probe mirror M is at an angle θ to the optical axis. The two beams return to the beam splitter BS and illuminate the CCD through lens L, where the CCD surface is conjugated with the reference mirror R. As the optical path lengths from R and M to the BS are almost the same, it can be assumed that M is imaged exactly on the CCD within the depth of the field. Thus, a virtual image M' of M is formed on the reference mirror side. The optical path difference (OPD) at the intersection of R and M' corresponds to zero, and the interference fringes can only be observed near the corresponding positions on the image plane, as shown in Fig. S1b. The obtained interference signal on the CCD appears to be enveloped within a thick line, whose width W is dependent on the polar angle θ, and the direction and position of this line reflect the azimuth angle φ and axial position D of the measuring plane.

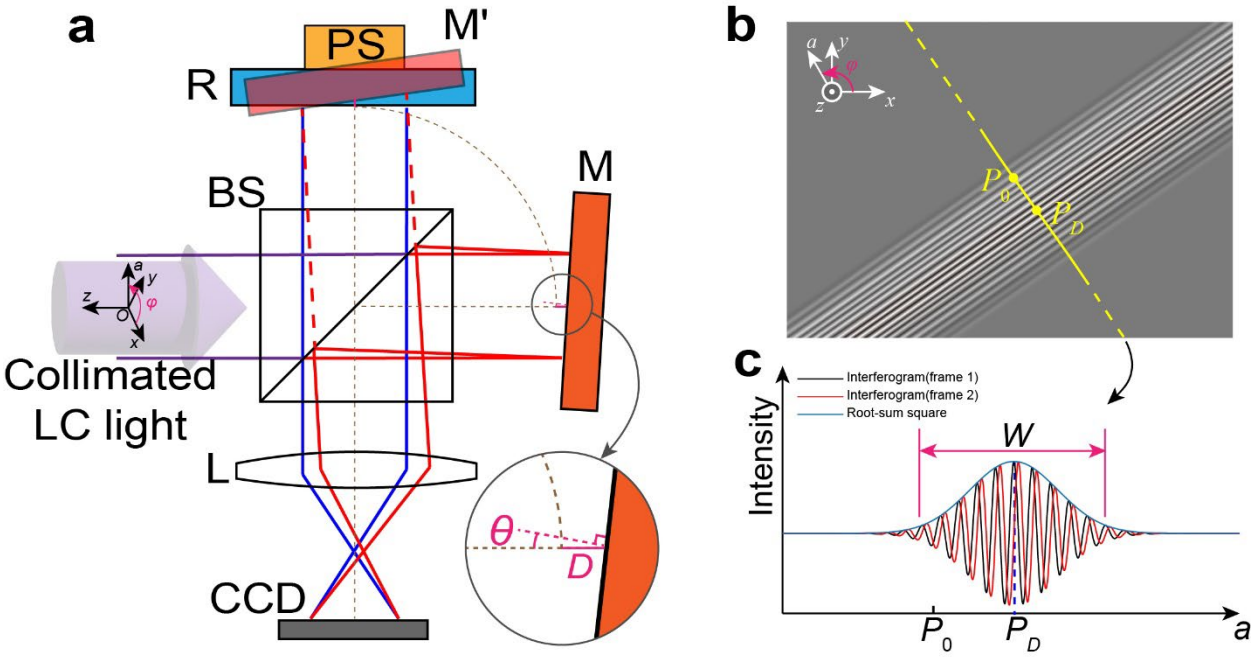

FIG.S1 Diagram of LCSI. a The 2D schematic of Twyman-Green-type LCSI, where the paper is always perpendicular to the axis of rotation of the measurement surface M. BS: beam splitter; M: probe mirror; R: reference mirror; L: imaging lens; CCD: charge-coupled device; PS: phase shifter. **b** Interference pattern captured on the CCD, where P_0 is the midpoint of the CCD and the yellow line corresponds to the image on the CCD. **c** One-dimensional distribution of the interference signal observed along the yellow line, where the black and red lines represent the interference signals of adjacent frames, and the blue line is the coherence envelope extracted based on their root-sum square. Note that figures (**b**) and (**c**) are the same as those in FIG.1 (b) and (c), as both configurations can achieve the same experimental phenomena, but the configuration in FIG.1 allows for the working distance to be adjusted freely.

However, extracting the envelope information directly from the interference pattern is difficult because of the interference carriers. A phase shifter (such as a PZT) can be placed at the reference mirror to construct a temporal phase-shifting function. The phase loaded on the phase shifter is related to the camera frame rate and causes a phase difference of exactly π/2 between adjacent frames, as shown in the two interferograms in Fig. S1c. After removing the DC component of the interference signal, the complete interference envelope was extracted as shown in Fig. S1c by the root-sum square of the orthogonal AC signals. The center position and width of the envelope can be quickly obtained using the centroid and root-mean-square methods, respectively. Therefore, the axial position D, polar angle θ, and azimuth angle φ of probe mirror M in the world coordinate system can be directly obtained by analyzing the shape of the low-coherence interference envelope on the CCD. The world coordinate system can be transformed into an object coordinate system via a coordinate transformation to obtain the three-DOF of the object (the axial position D, pitch angle θ_x and yaw angle θ_y).

Next is the detailed derivation of the measurement principle. Figure S2 is a schematic diagram of the interferometer in the *Oza* plane, which is extracted from the beam coordinate system *Oxyz*, where z is the opposite direction of the measurement light axis, and vector a is in the *Oxy* plane and makes an angle φ with the x-axis. The rotation of the test plane axis, which includes the pitch and yaw directions, can be fully expressed in the *Oza* plane. In Fig. S2a, the collimated LC light is split by a beam splitter (BS), with the reference light (blue line) vertically hitting the reference mirror (R) and returning along the same path. The measurement light (red line) hits the probe mirror at an angle θ with the wavefront and returns to the BS. Subsequently, the light reflected from R and M passes through the imaging lens L, and within the depth of field range, L projects the images of M and R onto a charge-coupled device (CCD). According to Fermat's principle, the optical path difference between the two light paths depends on the z-direction displacement. Because the optical path lengths from the center of the beam to R and M are the same, the two light beams imaged onto the CCD center p_0 are completely coherent and generate the strongest interference signal. Because of the existence of θ, different horizontal positions on the CCD correspond to different optical path differences; therefore, only a portion of the region is coherent on the image plane, and the width of the coherence region on the image plane, W, can be expressed as

$$W = Ac\frac{\tau}{2}\cdot\frac{1}{\tan\theta} \tag{S1}$$

where A represents the imaging transmittance, c represents the speed of light, and τ represents the coherence time of the light source.

When the position and orientation of M change, as shown in Fig. S2b, the angle between its surface and the measured wavefront decreases, leading to an increase in the coherence width W. In addition, the midpoint shifts along the optical axis by D. Based on the difference in the optical path lengths corresponding to different positions on the image plane, the position with the strongest interference p_D on the image plane becomes:

$$p_D = p_0 + \frac{AD}{\tan\theta} \tag{S2}$$

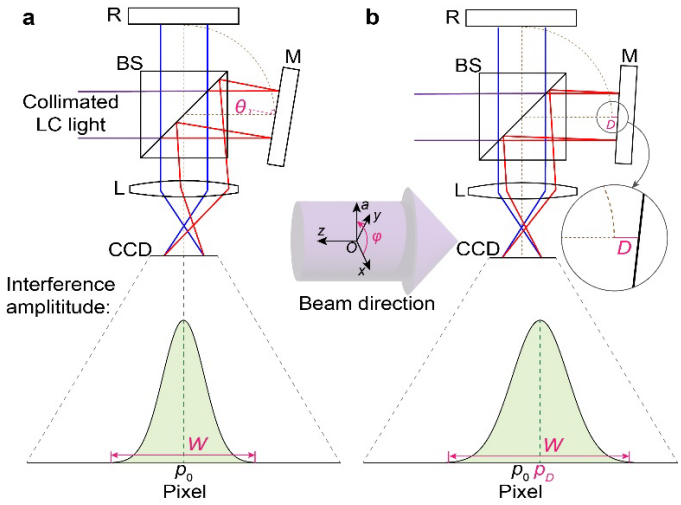

FIG.S2 Two-dimensional schematic diagram of LCSI, with the paper perpendicular to the rotation axis of the probe mirror. Panels **a** and **b** show the cases where the probe mirror has different positions and orientations.

The previous analysis was based on a two-dimensional space. To consider the situation of two beams of light in a three-dimensional space, the completely coherent area obtained on the CCD image plane comes from the intersection of two equal optical path planes, which is a straight line called the equal-optical-path line (EOPL), as shown in Fig. S3. The width of the coherence area that extended radially along the EOPL was precisely W, and the direction of the line was perpendicular to the azimuth angle φ between the planes. By selecting a row ($y = y_1$) and a column ($x = x_2$), two sets of coherence envelope distributions can be obtained: By extracting their midpoints (x_1, y_1), (x_2, y_2) and the coherence widths W_x and W_y, the value of φ and W can be obtained:

$$\varphi = \tan^{-1}\frac{y_2 - y_1}{x_2 - x_1} + \frac{\pi}{2}, \tag{S3}$$

$$W = W_x\left|\cos\varphi\right| = W_y\left|\sin\varphi\right|. \tag{S4}$$

Substituting Eq. (S4) into Eq. (S1), the polar angle θ between the optical axis and reference plane is obtained as

$$\theta = \tan^{-1}\left(\frac{Ac\tau}{2nW_x\left|\cos\varphi\right|}\right) = \tan^{-1}\left(\frac{Ac\tau}{2nW_y\left|\sin\varphi\right|}\right), \tag{S5}$$

where n represents the refractive index of the air. To obtain the distance D of the measurement point corresponding to pixel P_0, substitute the distance from P_0 to the EOPL into Eq. (S2) yields:

$$D = \frac{\left|\overline{P_0P_D}\right|}{A}\tan\theta\,. \tag{S6}$$

The positions and orientations of the test object are represented by the object coordinate system. When θ, φ, and D are all zero, the origin of the object coordinate system is at the center of the illuminated surface of the object, and the three axes are the same as those of the beam coordinate system $Oxyz$. When the object coordinate system is first rotated counterclockwise by an angle of θ_x about the x-axis and then rotated counterclockwise by an angle of θ_y about the y-axis, the rotation matrix relative to the original coordinates is as follows:

$$R = \begin{bmatrix} \cos\theta_y & 0 & -\sin\theta_y \\ 0 & 1 & 0 \\ \sin\theta_y & 0 & \cos\theta_y \end{bmatrix}\begin{bmatrix} 1 & 0 & 0 \\ 0 & \cos\theta_x & \sin\theta_x \\ 0 & -\sin\theta_x & \cos\theta_x \end{bmatrix}. \tag{S7}$$

The normal direction of surface M in the beam coordinate system $Oxyz$ is measured as:

$$\hat{m} = \begin{bmatrix}\sin\theta\cos\varphi & \sin\theta\sin\varphi & \cos\theta\end{bmatrix}^{\mathrm{T}}. \tag{S8}$$

This also corresponds to the z-axis direction of the object coordinate system; thus,

$$\begin{bmatrix}0 & 0 & 1\end{bmatrix}^{\mathrm{T}} = R\hat{m}\,. \tag{S9}$$

According to the above equation, θ and φ can be converted into pitch angle θ_x and yaw angle θ_y:

$$\theta_x = -\tan^{-1}\left(\tan\theta\sin\varphi\right), \tag{S10}$$

$$\theta_y = \sin^{-1}\left(\sin\theta\cos\varphi\right). \tag{S11}$$

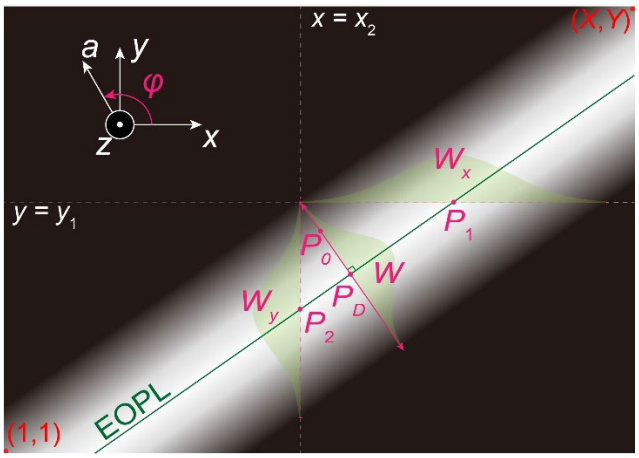

FIG.S3 Schematic diagram of coherence intensity distribution on the CCD plane.

Next, temporal phase shifting was used to extract the envelope information. The detected light intensity signal I at a certain pixel (x, y) on the image plane is modulated by the coherence envelope C and the interference phase α, i.e.,

$$I = I_R + I_M + 2C\sqrt{I_R I_M}\cos(\alpha), \tag{S12}$$

where I_R and I_M are the intensities of the measured and reference light, respectively, which can be measured in advance by blocking the other arm. C and α are functions of the optical path difference D. Because the measurement process concerns only the shape of the coherence envelope, temporal phase shifting is used to eliminate the influence of the interference phase α on the measurement and make the intensity signal become

$$I(t) = I_R + I_M + 2C\sqrt{I_R I_M}\cos\left(\alpha + \frac{\pi}{2} f_{\mathrm{FR}} t\right), \tag{S13}$$

where f_{FR} is the frame rate of the CCD, t is the time, and the additional term $\pi f_{\mathrm{FR}} t/2$ represents the orthogonality of the interference phase between frames during continuous acquisition. Let t_0 and t_1 be the acquisition times of two adjacent frames. C can be obtained using the root sum square of the alternating current component:

$$C = \sqrt{\frac{\left(I(t_0) - I_R - I_M\right)^2 + \left(I(t_1) - I_R - I_M\right)^2}{4 I_R I_M}}. \tag{S14}$$

The next step is to use the full-field distribution of C to calculate the EOPL equation and the coherence width W. Two sets of one-dimensional envelope distributions were obtained: $C(x, y_1)$ and $C(x_2, y)$ in row $y = y_1$ and column $x = x_2$, respectively. The one-dimensional distribution shape of C is usually symmetric, with a peak at the center of the envelope. Therefore, the centroid method can be used to locate it, which is expressed as follows:

$$x_1 = \frac{\sum_{x=1}^{X} xC\left(x, y_1\right)}{\sum_{x=1}^{X} x}, \tag{S15}$$

$$y_2 = \frac{\sum_{y=1}^{Y} yC\left(x_2, y\right)}{\sum_{y=1}^{Y} y}. \tag{S16}$$

where X and Y are the total numbers of pixels in the CCD in the horizontal and vertical directions, respectively. For this symmetrical distribution, the width corresponding to 68% of the area can be described by the double standard deviation 2σ used in statistics. Therefore,

$$W_x = \beta\mu\sigma_x = \beta\mu\sqrt{\frac{\sum_{x=1}^{X}\left[\left(x - x_1\right)C\left(x, y_1\right)\right]^2}{\sum_{x=1}^{X} C^2\left(x, y_1\right)}}, \tag{S17}$$

$$W_y = \beta\mu\sigma_y = \beta\mu\sqrt{\frac{\sum_{y=1}^{Y}\left[\left(y - y_2\right)C\left(x_2, y\right)\right]^2}{\sum_{y=1}^{Y} C^2\left(x_2, y\right)}}. \tag{S18}$$

The equation shows that β is a coefficient related to the spectral shape, and μ represents the size of the pixel, both of which are eliminated when solving for three degrees of freedom. According to Eq. (S3), the slope of EOPL is denoted as -cot φ, then EOPL can be expressed as:

$$y_{\mathrm{E}} = -\cot\varphi\left(x - x_1\right) + y_1. \tag{S19}$$

The actual distance from the image plane center P_0(X/2,Y/2) to the EOPL is given by

$$\left|\overline{P_0P_D}\right| = \mu\frac{\left|\cot\varphi\left(\frac{X}{2} - \frac{x_1 + x_2}{2}\right) + \left(\frac{Y}{2} - \frac{y_1 + y_2}{2}\right)\right|}{2\sqrt{\cot^2\varphi + 1}}. \tag{S20}$$

Using all the elements required for Eqs. (S6), (S10), and (S11), the three degrees of freedom of the image plane center (and, of course, any other point) can be determined using two LCSI patterns.

S3. System workflow

The system workflow is illustrated in Fig. S4. Figure S4a shows the overall operational flow. In the initial phase, the measurement arm and reference arm are sequentially blocked to acquire their respective background intensity images, which are later used to enhance the interferogram contrast during pose extraction. Subsequently, the repetition frequency of the laser is scanned to adjust the interference signal to the center of the CCD image. Once centered, a set of three-degree-of-freedom (3-DOF) measurement results is obtained using the extraction algorithm described in Section S2. However, the zero reference of this initial result is virtual. Therefore, the absolute 3-DOF values are determined by calculating the absolute axial distance at pulse-to-pulse alignment based on the repetition frequency of the femtosecond laser.

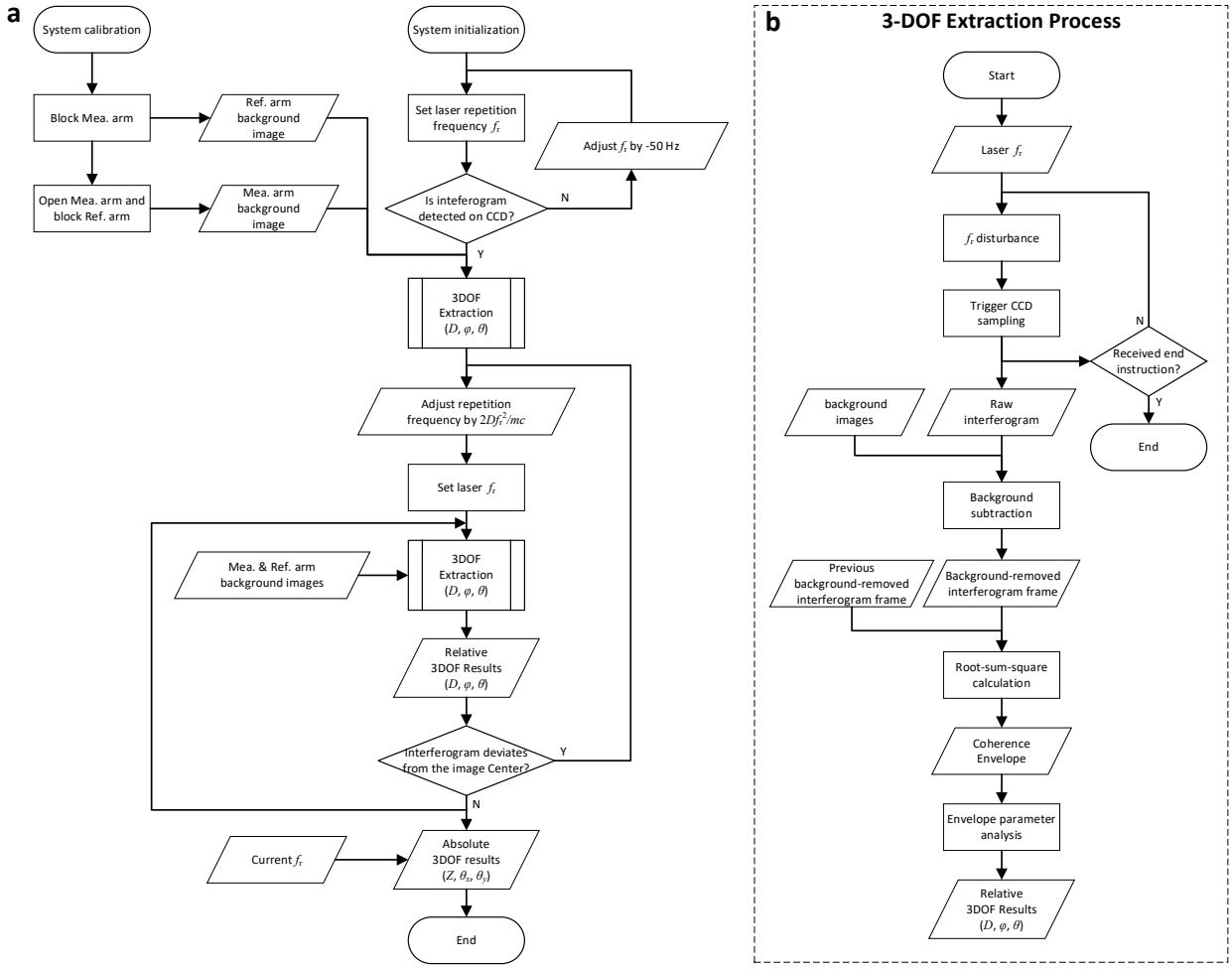

FIG.S4 System workflow diagram: a Global workflow diagram; **b** 3-DOF extraction algorithm.

Figure S4(b) details the 3-DOF extraction process from the captured interferograms. After setting the laser repetition frequency, a slight disturbance is applied to the frequency to induce a temporal phase shift. The CCD is then triggered to acquire raw interferogram frames. Following background subtraction, each interferogram frame is processed by removing the residual background using the previous frame, and the root-sum-square of the orthogonal signals is calculated to extract the coherence envelope. Finally, envelope parameter analysis is performed to obtain the relative 3-DOF results.

S4. Repetition frequency control

The locking loop for repetition frequency control is illustrated in Fig. S5a. The resonator output is directly detected by a photodetector (PD). After passing through a 60 MHz ± 10 MHz band-pass filter, the fundamental frequency is isolated and amplified by a radio-frequency (RF) amplifier to approximately 0 dB. This amplified signal is then mixed with a standard RF signal generated by a signal generator, and the resulting error signal passes through a 5 MHz low-pass filter into a PID controller (LB1005). The PID output signal is linearly amplified by a high-voltage amplifier, which drives a piezoelectric transducer (PZT) within the resonator to adjust the optical fiber length, thereby closing the frequency-locking loop. The Allan deviation after repetition frequency locking is shown in Fig. S5b. The repetition frequency stability of the laser reaches 2×10^{-12} at 1-second gate time, surpassing the precision of the frequency reference (SRS SIM940, accuracy: 5×10^{-11}, stability: 2×10^{-11} at 1 second), thus ensuring reliable tracking performance.

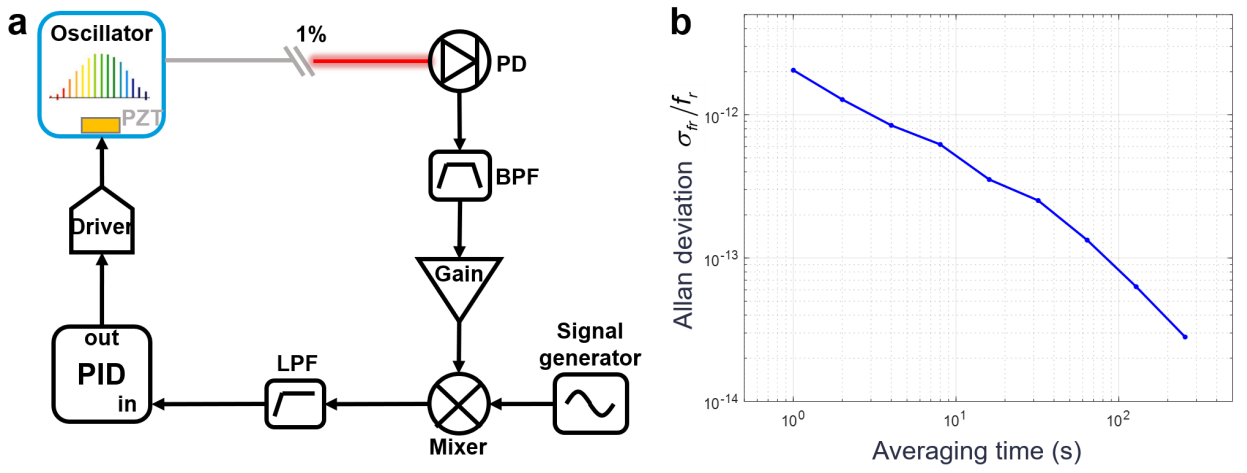

FIG.S5 Schematic diagram of repetition frequency locking: a locking loop; **b** Allan deviation.

S5. Fitting coherence time τ

The results of the polar angle θ measurement can be traced back to the coherence time τ of the light source, specifically $\tan\theta = 2W/Ac\tau$, where the imaging transmittance A is equal to 1 and c is the speed of light in vacuum. Based on the spectral shape and pixel size μ= 15 μm, the conversion between coherence width W and root-mean-square width W_{rms} is given by $W = \beta\mu W_{\mathrm{rms}}$, where β is a spectral coefficient that does not affect the calculation of three-DOF. We continuously vary the yaw angle and measure it, while simultaneously calibrating the angle change $\Delta\theta$ of each rotation using an autocollimator. After many measurements, the initial angle θ_0 and the parameter τ/β related to the coherence time can be fitted using the above formula. This process is illustrated in Fig. S6. It can be observed that LCSI can obtain results consistent with the theory within a dynamic range of 1000 arcsec, and the absolute angles can be determined within this range. When the angle between the interference arms is too large, the spatial interference fringes become denser, and downsampling of the pixels concerning the fringes reduces the signal contrast, affecting the measurement results. When the angle between the mirrors is too small, the envelope exceeds the field of view, making it impossible to accurately measure W_{rms}.

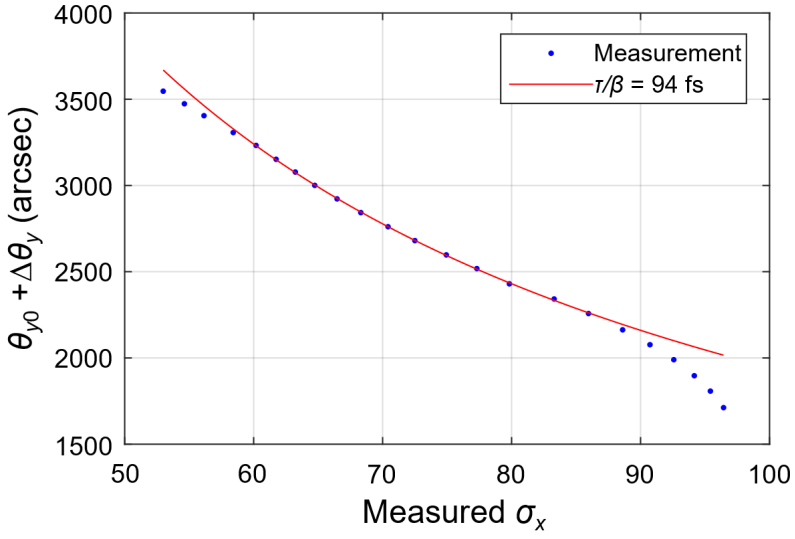

FIG.S6 Fitting result of the coherence time of the light source.

S6. Calibration of imaging magnification factor *A*

The magnification factor *A* of the imaging system is calibrated by measuring known geometric features and calculating the corresponding scale based on image dimensions. Typically, two methods can be employed for calibration: one is directly capturing an image of a grid board or resolution target with known dimensions (with grid dimension errors typically better than 0.2 μm) and calculating the magnification factor by dividing the real grid size by the corresponding CCD image size; the other is placing the target on a linear translation stage perpendicular to the optical axis, and calculating the magnification factor from the stage displacement feedback divided by the measured image displacement. The second method was used in our calibration, as illustrated in Fig. S7a. The linear translation stage (Thorlabs, LNR25M/M) driven by a micrometer (Thorlabs, DRV517) was manually displaced by increments of 100 μm, totaling 1 mm. After each displacement, the image displacement was extracted using the Scale-Invariant Feature Transform (SIFT) algorithm [50], as depicted in Fig. S7b. The calibration results are shown in Fig. S7c. A linear fit provided the magnification factor A = 0.9863, with a coefficient of determination R^2 = 0.99998 and a relative uncertainty $u(A)$ = 0.0016.

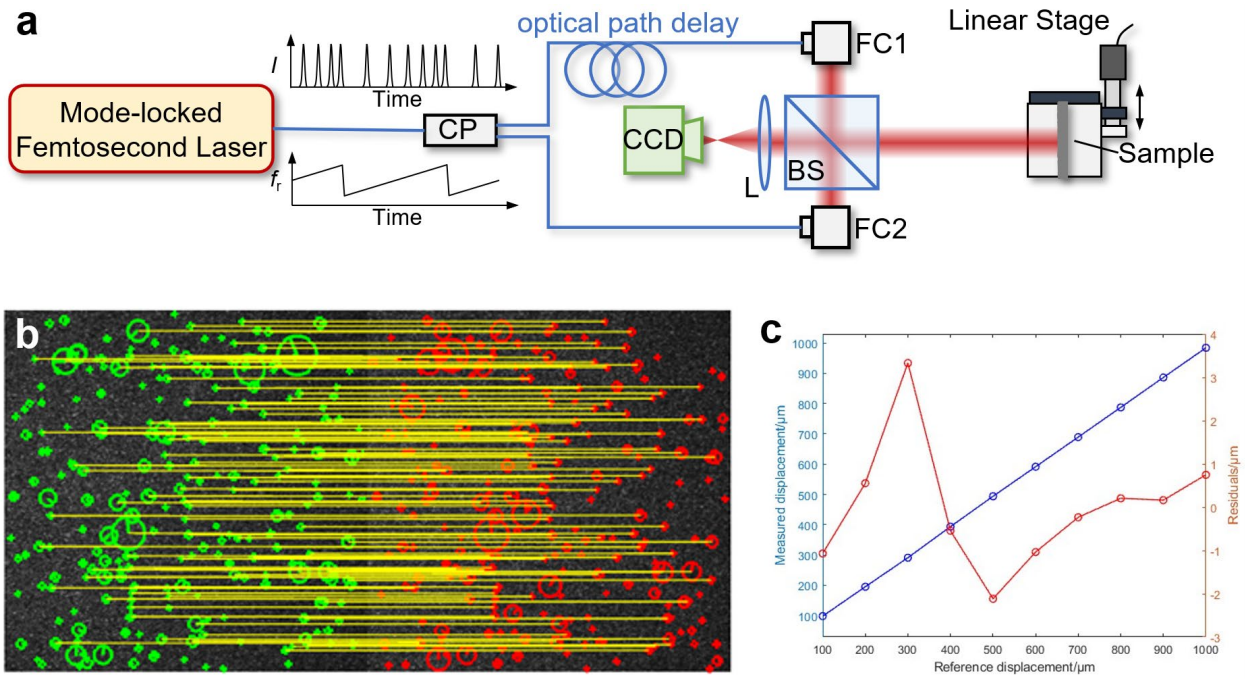

FIG.S7 Magnification factor calibration. a Experimental setup; **b** Illustration of image registration algorithm, with green and red circles indicating interest points identified before and after target motion, and yellow lines representing computed matches between corresponding points; **c** Comparison between measured displacements and reference values.

According to Eq. (S1), the magnification factor error primarily affects the polar angle θ measurement uncertainty, which is expressed as:

$$u(\theta) = \frac{\tan\theta}{A\left(1+\tan^2\theta\right)} u(A). \tag{S21}$$

The resulting uncertainty distribution within a 1000" measurement range is depicted in Fig. S8. It can be approximated that the relative uncertainty of the polar angle caused by magnification errors is comparable to the uncertainty of the magnification factor itself. For distance measurements, the system frequently updates the central repetition frequency to ensure pulse alignment at the image center, effectively correcting axial distance errors. Thus, the impact of polar angle errors on distance measurements is minimal and can be neglected.

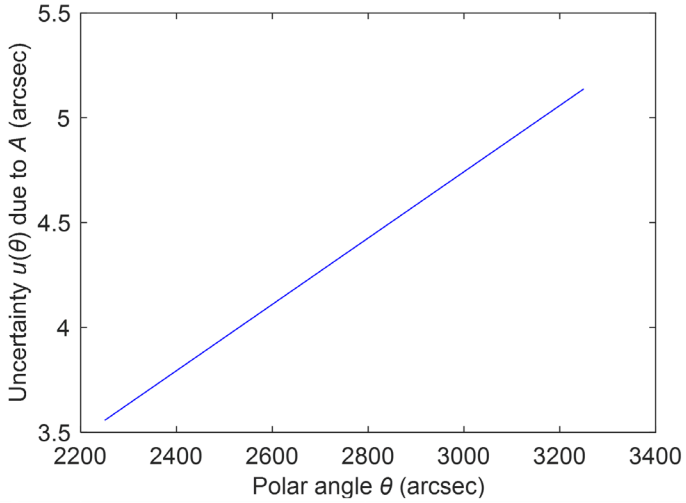

FIG.S8 Uncertainty in polar angle caused by magnification factor errors.

Reference

[50] Lindeberg, T. Scale Invariant Feature Transform. *Scholarpedia* **7**(5), 10491 (2012).

S7. Comparison between rms method and Gaussian fitting method

In this study, the root-mean-square (rms) method was used to determine the envelope width W. Unlike the commonly used Gaussian fitting method, the rms method is very fast and has better repeatability when the conditions for extracting the complete envelope are met. For comparison, 500 frames of data in the experiment were selected as shown in Fig. S9a, averaging 100 lines per frame to measure the envelope width W using both methods. The relative deviation in measuring the envelope width using the RMS and Gaussian fitting methods is denoted as ε_{rms} and ε_{Gauss}, respectively, and their results are shown in Fig. S9b. The results indicated that the RMS method exhibited better repeatability than the Gaussian fitting method. Additionally, the RMS method only takes 0.88 seconds to complete all calculations, while the Gaussian fitting method takes as long as 2198.17 seconds (using a personal computer, i7-10700KF, 32G, MATLAB2020b).

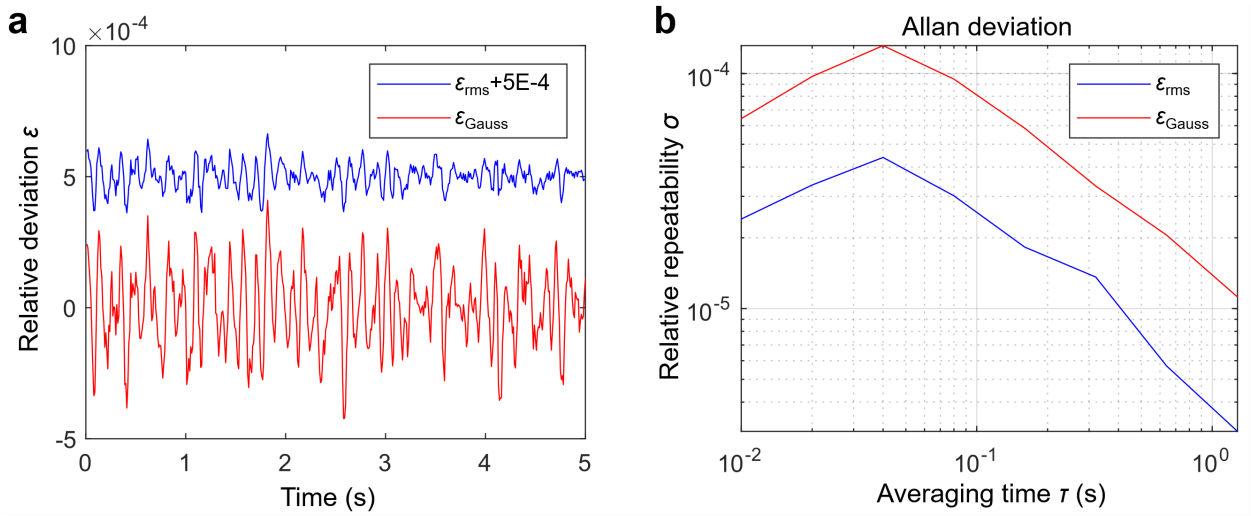

FIG.S9 The results of measuring the coherence envelope width using two different methods. a The time-domain plot of the relative measurement deviation; **b** the Allan deviation of the two methods.

S8. Multi-target measurement sample

To verify the multi-target measurement functionality, a segmented mirror model composed of three hexagonal sub-apertures was used, as shown in Figure S10. Such structures are commonly found in synthetic aperture telescopes, and they typically have a large radius of curvature, allowing them to be considered as flat within a small field of view. In this model, each hexagonal surface has a side length of 17.3 mm and is supported by three bearings. At the center of the synthesized plane, one piezoelectric transducer (PZT) simultaneously supports all three surfaces. The PZT used can handle a maximum load voltage of 120 V and has a travel range of 20 μm. In the experiment described in Section 2.4, the applied signal was $U = 30+15\sin(10\pi t)$, where t represents time in seconds and U is in volts.

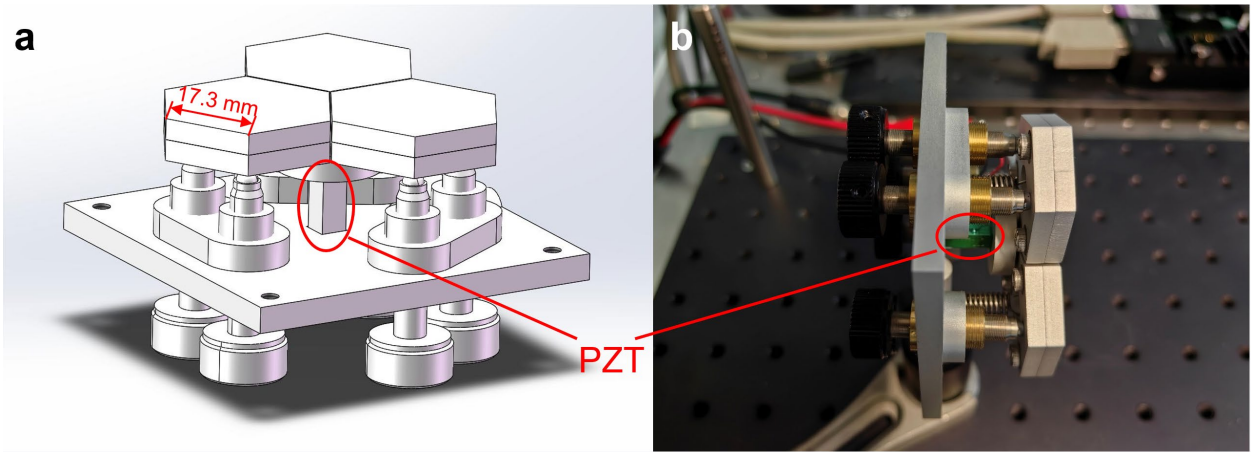

FIG.S10 Segmented mirror model. a Three-dimensional structural diagram; **b** Side view photo of the model.

Supplementary video information

This video showcases the real-time measurement of a ground glass surface using low-coherence spatial interferograms. The imaging transmittance used in the experiment is 0.57, and the camera frame rate is 100 Hz. The ground glass is fixed on a six-axis piezoelectric displacement stage, which randomly changes its position and orientation at a speed of 2 Hz.

The video is divided into four sections:

Top left: The original interferogram image.

Top right: The coherent envelope extracted from two-frame phase-shifted interferograms.

Bottom left: The reconstructed 3D surface pose, with the corresponding initial biases subtracted.

Bottom right: Independent measurement results of 3-DOF.